Development of a distributed biosphere hydrological model and its evaluation with the Southern Great Plains Experiments (SGP97 and SGP99)

Lei Wang,[1] Toshio Koike,[1] Kun Yang,[2] Thomas J. Jackson,[3] Rajat Bindlish,[3] and Dawen Yang[4]

[1] A distributed biosphere hydrological model, the so-called water and energy budget-based distributed hydrological model (WEB-DHM), has been developed by fully coupling a biosphere scheme (SiB2) with a geomorphology-based hydrological model (GBHM). SiB2 describes the transfer of turbulent fluxes (energy, water, and carbon fluxes) between the atmosphere and land surface for each model grid. The GBHM redistributes water moisture laterally through simulating both surface and subsurface runoff using grid-hillslope discretization and then flow routing in the river network. The WEB-DHM was calibrated and validated for the Little Washita Basin using field observations from Southern Great Plains Hydrology Experiments (SGP97 and SGP99). For the SGP97 period, the model was calibrated and it shows an ability to reproduce point-scale energy fluxes (RMSE < 50 W m^{-2}) as well as CO_2 flux (RMSE = 4.6 μ mol m^{-2}s^{-1}). At basin scale, the WEB-DHM can simulate a reasonable hydrograph (Nash = 0.956) and spatial soil moisture distribution with calibration of only a few soil hydraulic parameters for discharge. The model was then validated using SGP99 data sets and observed discharge. For the validation period, the model shows good performance in reproducing the soil surface temperature at 11 sites and the spatial distribution of surface soil moisture, as well as long-term discharges (Nash = 0.715) in the hydroyear from 1 September 1998 to 31 August 1999 that covers both the annual largest flood peak of 1999 and the SGP99 period. To our knowledge, this work is the first to undertake the development and evaluation of a distributed biosphere hydrological model using such comprehensive field observations.

1. Introduction

[2] Global climate changes have significant impacts on regional river runoff and water availability, which is most important for water resource managers and policy makers. It is reported that by 2050, drought-affected areas will likely increase in some water-stressed regions while flood risks are likely to increase in some wet areas [*Intergovernmental Panel on Climate Change*, 2007]. Under this circumstance, it is critical to integrate the knowledge of atmosphere and hydrology communities for improved prediction capability of available water resources and possible hazards (floods and droughts).

[3] Distributed hydrological models (DHMs) can give distributed representation of the spatial variation and physical descriptions of runoff generation and routing in river channels from basin to continental scales. DHMs have been developing rapidly since the original blueprint of *Freeze and Harlan* [1969] for a physically based distributed model. Over last 20 years, a number of DHMs incorporating new techniques appeared such as SHE [*Abbott et al.*, 1986; *Bathurst et al.*, 1995], the distributed triangulated irregular network model [*Ivanov et al.*, 2004], and the geomorphology-based hydrological model (GBHM) [*Yang*, 1998; *Yang et al.*, 2000, 2004; *Wang et al.*, 2006]. Though improvements over the lumped hydrological models have been made by representing spatial heterogeneity, DHMs have large uncertainties in simulating water exchanges at the soil-atmosphere interface and the time evolution of surface soil moisture owing to the conceptual treatment of the land surface.

[4] On the other hand, over the last several decades, land surface models (LSMs) have evolved from simple bucket

[1]Department of Civil Engineering, University of Tokyo, Tokyo, Japan.
[2]Institute of Tibetan Plateau Research, Chinese Academy of Sciences, Beijing, China.
[3]Hydrology and Remote Sensing Laboratory, ARS, USDA, Beltsville, Maryland, USA.
[4]Department of Hydraulic Engineering, Tsinghua University, Beijing, China.

models without vegetation consideration [e.g., *Manabe*, 1969] into credible representations of water and energy fluxes in soil-vegetation-atmosphere-transfer (SVAT) systems [e.g., *Sellers et al.*, 1986, 1996a; *Dickinson et al.*, 1986, 1998; *Verseghy*, 1991; *Milly*, 1992; *Liang et al.*, 1994; *Koster and Milly*, 1997; *Mengelkamp et al.*, 1999; *Dai et al.*, 2003]. The physical basis of LSMs makes them an attractive alternative to the conceptual types of ET models that have traditionally been applied in hydrological modeling. However, many of them only include elementary runoff components of infiltration excess and gravitational outflow, without considering the subgrid variability of topography and lateral water flow processes [*Henderson-Sellers et al.*, 1993]. Recently, the lack of descriptions of regional groundwater aquifers has been recognized as another drawback of current LSMs, especially in humid areas with shallow water tables [*Yeh and Eltahir*, 2005], since groundwater-atmosphere interaction has a potentially significant influence on spatial and temporal climate variability [*Maxwell et al.*, 2007].

[5] Furthermore, the prediction of regional or basin-scale surface soil moisture distribution should be improved, since the spatial distribution of land surface wetness has been recognized as one of the most important factors representing the land surface heterogeneity, which can significantly affect the energy and water fluxes simulated in atmospheric models [e.g., *Fast and McCorcle*, 1991; *Li and Avissar*, 1994; *Chen and Avissar*, 1994; *Avissar et al.*, 2004]. Many studies showed that estimates of soil moisture and its spatial distribution with good accuracy are critical for atmospheric model forecasts [e.g., *Leese et al.*, 2001; *Pielke*, 2001; *Findell and Eltahir*, 2003]. However, owing to the one-dimensionality of most current LSMs (e.g., SiB2), lateral soil moisture redistributions due to topographically driven runoff were usually not well formulated since they were originally developed for application in general circulation models (GCMs).

[6] The coupling of LSMs and DHMs potentially improves the land surface representation, benefiting both the streamflow prediction capabilities of the hydrological models as well as providing improved estimates of water and energy fluxes into the atmosphere [*Pietroniro and Soulis*, 2003; *Yu et al.*, 2006]. Meanwhile, carbon dioxide uptake and evaporation by vegetation are intrinsically coupled, leading to links and feedbacks between land surface and climate [*Hutjes et al.*, 1998]. Therefore, it is more realistic to select an LSM that incorporates the canopy photosynthesis-conductance model to describe the simultaneous transfer of CO_2 and water vapor into and out of the vegetations, such as SiB2 [*Sellers et al.*, 1996a] or the revised BATS [*Dickinson et al.*, 1998], to couple with a DHM for biosphere hydrological modeling. *Tang et al.* [2006] have developed a distributed biosphere hydrological model that can continuously simulate land-atmosphere interactions via exchanges of water, energy, and carbon at the basin scale in a spatially distributed manner. Though the model has been successfully applied in impact studies [see *Tang et al.*, 2007, 2008], until now, this model has not been comprehensively evaluated against integrated field observations including not only discharges but also fluxes and soil moisture measurements owing to a lack of data sets for continental-scale river basins.

[7] In this study, a new distributed biosphere hydrological model has been developed and evaluated using comprehensive field observations from the Southern Great Plains Hydrology Experiments (SG97 [*Jackson et al.*, 1999] and SGP99 [*Jackson and Hsu*, 2001]). The simple biosphere model 2 (SiB2 [*Sellers et al.*, 1996a]) with advanced physics, and the grid-based GBHM [*Yang et al.*, 2004] with spatially distributed structure and physical runoff and river routing schemes, have been selected to develop the distributed biosphere hydrological model incorporating subgrid topography, which is referred to as the water and energy budget-based distributed hydrological model (WEB-DHM [*Wang*, 2007]). The model can give consistent descriptions of water, energy and CO_2 fluxes at a basin scale. Validation of the new coupled model needs various data sets, including those of discharge, energy and CO_2 fluxes, as well as soil moisture and temperature data sets. The Southern Great Plains Hydrology Experiments (SG97 [*Jackson et al.*, 1999] and SGP99 [*Jackson and Hsu*, 2001]) provide us a good opportunity to evaluate the coupled model against various observations with reliable accuracy [see also *Rigon et al.*, 2006; *Bertoldi et al.*, 2006]. The WEB-DHM is calibrated during the SGP97 period and validated during the SGP99 period in the Little Washita Basin. This paper describes the development of the WEB-DHM and its evaluation using the SGP97 and SGP99 data sets.

2. Model Structure

[8] This section describes the overall structure of the WEB-DHM and the subgrid parameterization as well as the soil structure in the model.

2.1. Overall Structure

[9] The overall model structure is shown in Figure 1 and can be described as follows.

[10] 1. A digital elevation model (DEM) is used to define the target area and then the target basin is divided into subbasins (see Figure 1a).

[11] 2. Within a given subbasin, a number of flow intervals are specified to represent time lag and accumulating processes in the river network according to the distance to the outlet of the subbasin. Each flow interval includes several model grids (see Figure 1b).

[12] 3. For each model grid with one combination of land use type and soil type, the SiB2 is used to calculate turbulent fluxes between the atmosphere and land surface independently (see Figures 1b and 1d).

[13] 4. The GBHM is used to calculate the runoff from a model grid with a subgrid parameterization. Each model grid is subdivided into a number of geometrically symmetrical hillslopes (see Figure 1c), which are the basic hydrological units (BHUs) of the WEB-DHM. For each BHU, the GBHM is used to simulate lateral water redistributions and calculate runoff (see Figures 1c and 1d). The runoff for a model grid is the total response of all BHUs in it.

[14] 5. For simplicity, the streams located in one flow interval are lumped into a single virtual channel in the shape of trapezoid. All the flow intervals are linked by the river network generated from the DEM. All the runoff from the model grids in the given flow interval is accumulated into the virtual channel and led to the outlet of the river basin.
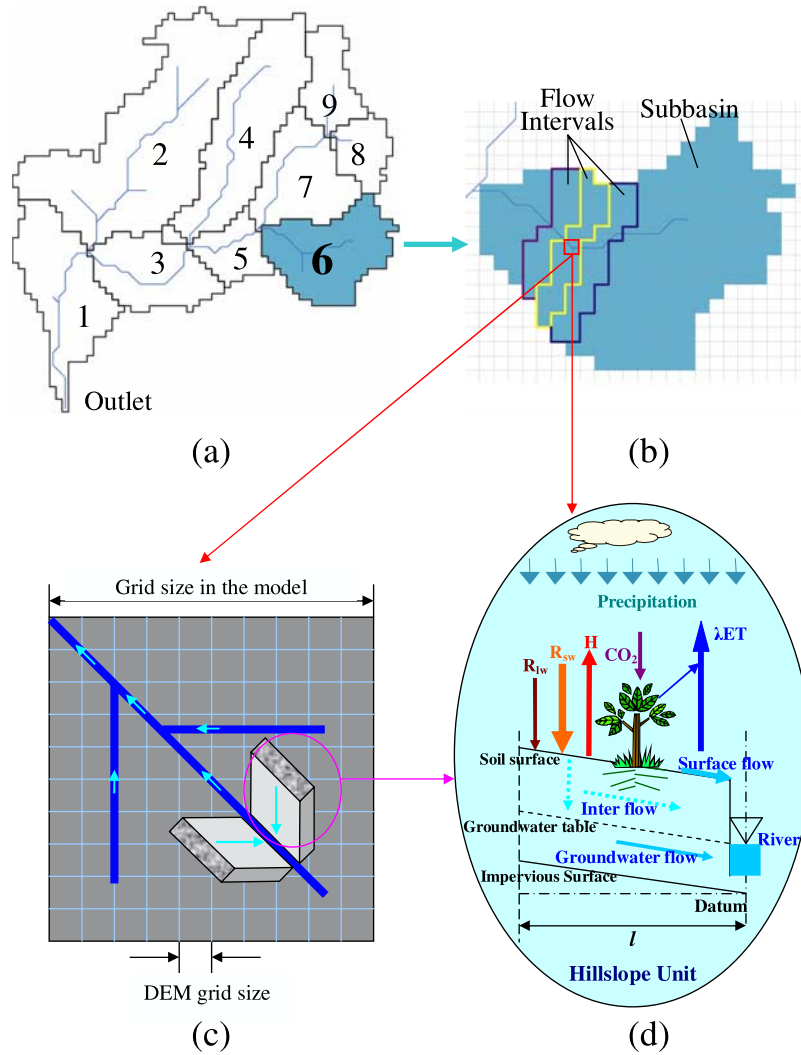
Figure 1. Overall structure of the WEB-DHM: (a) division from a basin to subbasins, (b) subdivision from a subbasin to flow intervals comprising several model grids, (c) discretization from a model grid to a number of geometrically symmetrical hillslopes, and (d) process descriptions of water moisture transfer from the atmosphere to river. Here the SiB2 is used to describe the transfer of the turbulent fluxes (energy, water, and CO_2 fluxes) between the atmosphere and land surface for each model grid, where R_{sw} and R_{lw} are downward solar radiation and longwave radiation, H is the sensible heat flux, and λ is the latent heat of vaporization. The GBHM simulates both surface and subsurface runoff using grid-hillslope discretization, and then simulates flow routing in the river network.

[15] It should be mentioned that, for simplicity and reducing computation costs, the interactions of groundwater between flow intervals are not considered in the model. Furthermore, within a flow interval, the lateral moisture exchanges between model grids are not formulated. There-fore, the model can maintain high efficiency for simulations of large-scale river basins while incorporating subgrid topography. This is because the WEB-DHM inheriting the spatial structure of GBHM employs the catchment function and width function to lump the topography [see *Yang et al.*, 2000] and integrates the BHUs within one large model grid using a subgrid parameterization.

2.2. Subgrid Parameterization

[16] When a fine DEM is available and simulation is performed in larger model grids, a subgrid parameterization scheme is used to capture topographical characteristics. Each BHU (hillslope) is actually a conceptual element in a large model grid (Figure 1c). The hillslope parameters (length and slope) for each model grid are obtained by preprocessing of the fine DEM.

[17] As illustrated in Figure 1c, it is assumed that a large model grid comprises a set of symmetrical hillslopes located along the streams. Within a model grid, all hillslopes are viewed as being geometrically similar. A hillslope with unit width is a BHU and is represented by a rectangular inclined plane. The hillslope length within a model grid is calculated as

$$l = A/2 \sum L, \qquad (1)$$

where A is the model grid area and $\sum L$ is the total length of streams within the model grid extracted from the fine DEM.
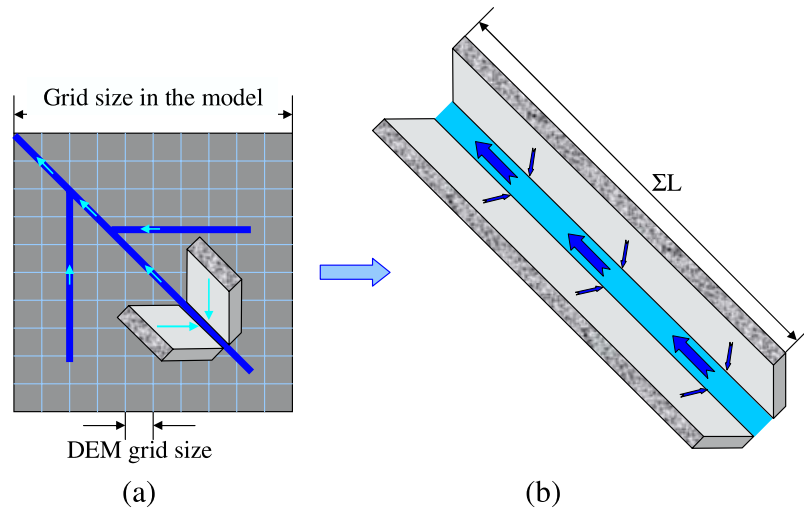
Figure 2. Simplification of streams in a model grid from (a) the DEM derived streams with a total length of $\sum L$ to (b) one stream with a length of $\sum L$, which flows along the main flow direction of the model grid. Here a couple of geometrically symmetrical hillslopes are assumed to be located along one stream in both Figures 2a and 2b.

The total river length $\sum L$ decreases with increasing threshold area [*O'Callaghan and Mark*, 1984; *Tarboton et al.*, 1991]. The model grid slope is taken to be the mean of all subgrid slopes in the fine DEM.

[18] All streams extracted from the fine DEM within a given model grid (see Figure 2a) can be simplified as one stream with a length $\sum L$ (see Figure 2b) flowing along the main flow direction of the model grid. Therefore, the total runoff generated from a given model grid can be regarded as being from the new hillslopes along the single stream.

2.3. Soil Model

[19] For each model grid, the initial depth of the unsaturated zone (Ds; see Figure 3) is usually defined according to the average slope of the model grid owing to a lack of geological data. It is assumed that a steeper slope results in lower Ds. Two different soil subdivision schemes are used in describing land surface processes and hydrological processes.

[20] In the calculation of land surface processes, the three-layer soil structure for the unsaturated zone is the same as that in SiB2. The depth of the first layer (D_1) is defined as 5 cm, while the root depth ($D_1 + D_2$) could be defined according to vegetation type by SiB2 default. The thickness of the deep soil zone (D_3) changes with fluctuation of the water table and is equal to the depth of the groundwater level minus the thickness of the upper two layers.

[21] In the simulation of soil water flow, a multiple-sublayer soil structure is employed to describe the unsaturated zone. In the model, the nonuniform vertical distribution is represented using an assumption of exponentially decreasing hydraulic conductivity with increasing soil depth given by $k_z = k_{surface} * \exp(-f * z)$ [*Cabral et al.*, 1992; *Robinson and Sivapalan*, 1996], where $k_{surface}$ and k_z are hydraulic conductivities at the soil surface and depth z, and f is a decay factor. The surface layer with a depth D_1 is kept as the first layer. The root zone and deep soil zone are uniformly subdivided into several sublayers. As shown in

Figure 3, the multiple-sublayer structure is employed to calculate vertical interlayer flows and lateral runoff.

[22] For each model grid, the soil moisture contents of sublayers are transferred from/to the soil moisture contents in the first layer (W_1), root zone (W_2) and deep soil zone (W_3) following mass conservation. First, the SiB2 simulates vertical processes and updates ground interception and
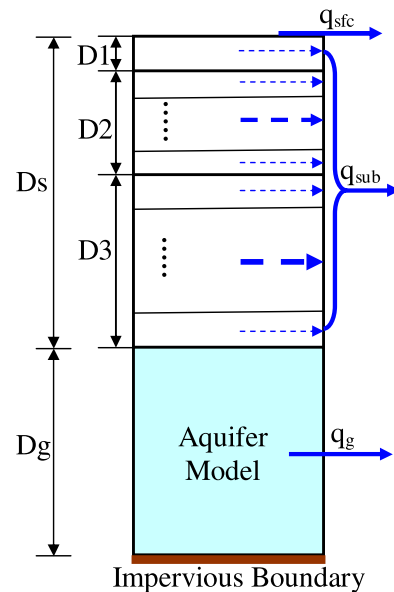

Figure 3. Soil model of the WEB-DHM. Two different soil subdivision schemes are used in describing the land surface and hydrological processes. The three-layer soil structure used in SiB2 is kept to represent the unsaturated zone in the calculation of land surface processes, and the unsaturated zone is divided into multiple sublayers when simulating vertical interlayer moisture exchanges and lateral subsurface runoff, as well as recharge from the groundwater aquifer.

surface wetness (W_1). Second, vertical interlayer water exchanges and lateral subsurface flows, as well as groundwater recharge and discharge to the river channel, are simulated to redistribute sublayer soil moisture. Third, after the update of soil moisture within the vertical soil profile, the groundwater level is changed with the soil moisture change of the lowest sublayer within the unsaturated zone. Finally, W_1, W_2 and W_3 are recalculated from the updated sublayer soil moisture for the simulation in the next time step.

[23] In this new soil model, the van Genuchten equation [*van Genuchten*, 1980] used by the GBHM is kept as the soil hydraulic function for the WEB-DHM and the Campbell/Clapp-Hornberger parameterization [*Campbell*, 1974; *Clapp and Hornberger*, 1978] used in SiB2 is not inherited. This is because *Braun and Schadler* [2005] have shown the van Genuchten/Rawls-Brakensiek model [*van Genuchten*, 1980; *Rawls and Brakensiek*, 1982] is superior to the Campbell/Clapp-Hornberger model in simulating soil water contents.

3. Model Processes

[24] The land-atmosphere interactions formulated by SiB2 have been presented by *Sellers et al.* [1996a]. Here, the descriptions of lateral water redistribution due to topographical effects are given in detail, including the runoff generation from the BHUs and flow routing in the river network.

3.1. Runoff From a Model Grid

[25] As we defined before, each model grid is represented by a number of BHUs. Lateral runoff generations are described on the BHU scale and then the runoff from a model grid is calculated.

3.1.1. Unsaturated Zone Water Flow

3.1.1.1. Vertical Interlayer Flow

[26] The vertical interlayer flows in the unsaturated zone are described using a one-dimensional Richards equation

$$\frac{\partial \theta(z,t)}{\partial t} = -\frac{\partial q_{vertical}}{\partial z} + r(z,t), \tag{2}$$

where t is time, z is the distance from the surface with positive values increasing vertically downward (m), $\theta (z, t)$ is the volumetric water content, $r (z, t)$ is the source or sink (i.e., evaporation and transpiration), and $q_{vertical}$ is the soil moisture fluxes in the vertical direction ($m^3 s^{-1} m^{-2}$), given as

$$q_{vertical} = -K(\theta, z)\left[\frac{\partial \psi(\theta)}{\partial z} - 1\right], \tag{3}$$

where $K (\theta, z)$ is hydraulic conductivity (m s^{-1}) and $\psi (\theta)$ is capillary suction (m).

[27] The Richards equation is solved by an implicit numerical solution scheme. After the vertical interlayer water moisture exchanges, saturated excess and recharge to groundwater are obtained at the upper and lower boundaries of the unsaturated zone.

3.1.1.2. Subsurface Flow

[28] For all the unsaturated sublayers above the groundwater level, the subsurface flow rate in sublayer i ($q_{sub} (i)$; m^3 s^{-1} m^{-1}) is calculated as

$$q_{sub}(i) = \begin{cases} K(\theta_i) * \sin \beta * \Delta z_i, & \theta_i > \theta_f, \\ 0, & \theta_i \leq \theta_f, \end{cases} \tag{4}$$

where $K(\theta_i)$ is the hydraulic conductivity (m s^{-1}) in sublayer i, Δz_i is the thickness (m) of sublayer i, and β is the slope of the model grid. The total subsurface flow (q_{sub}; m^3 s^{-1} m^{-1}) is the summation of q_{sub} (i) from all sublayers in the unsaturated zone.

3.1.2. Groundwater Flow

[29] Groundwater aquifers are treated as individual storage units corresponding to each model grid. All BHUs in a given model grid share the same groundwater level; while the BHUs in the same flow interval share the same river water level, since only one virtual channel was allocated for each flow interval. On the BHU scale, the exchange between the groundwater and river water (q_g; m^3 s^{-1} m^{-1}) is calculated using Darcy's law following *Yang et al.* [2000].

3.1.3. Surface Flow

[30] The surface water storage (M_{gw}; m) of each model grid is generated owing to the infiltration excess and saturation excess. The surface hillslope flow is described by steady constant sheet flow using Manning's equation

$$q_{sfc} = \frac{1}{n_s}(\sin \beta)^{1/2}\left(M_{gw} - M_{gw_{max}}\right)^{5/3}, \tag{5}$$

where q_{sfc} is the surface runoff of one simulation unit (m^3 s^{-1} m^{-1}); n_s is Manning's roughness parameter; $M_{gw_{max}}$ is maximum surface water storage (m).

[31] The total runoff generated from a BHU (q_{BHU}; m^3 s^{-1} m^{-1}) is calculated as

$$q_{BHU} = q_{sub} + q_g + q_{sfc}. \tag{6}$$

Therefore, the runoff from a model grid (q_{grid}; m^{3}s^{-1}) is the total runoff from all BHUs within the model grid

$$q_{grid} = 2\sum L * q_{BHU} = q_{BHU} * A/l. \tag{7}$$

3.2. River Routing

[32] As stated previously, a virtual channel is allocated for each flow interval. Therefore, the river networks of a subbasin are simplified such that only the main river is considered. The flow sequences among these simplified main rivers are defined by the codes of the divided subbasins [*Verdin and Verdin*, 1999] (see also O. Pfafstetter, Classification of hydrographic basins: Coding methodology, 1989, unpublished manuscript, Departamento Nacional de Obras de Saneamento). The lateral inflow into the main river from each flow interval ($q_{Lateral}$; m^3 s^{-1}) is the total runoff generated from all the model grids ($\sum q_{grid}$; m^3 s^{-1}) within the same flow interval. The flow routing of all the river networks in the basin is modeled using the kinematic wave approach

$$\frac{\partial Q}{\partial x} + \frac{\partial A_r}{\partial t} = \frac{q_{Lateral}}{L_f} \tag{8}$$

$$Q = \frac{S_0^{1/2}}{n_s p^{2/3}} \cdot A_r^{5/3}, \tag{9}$$

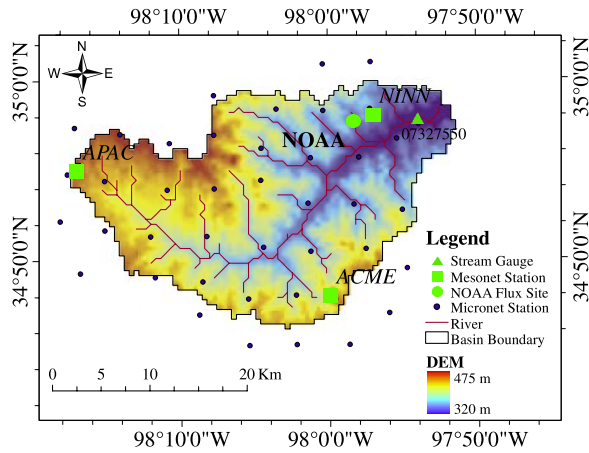where x is the distance along the longitudinal axis of the river (m), t is time (s), A_r is cross-sectional area (m^2), Q is

Figure 4. The Little Washita Basin.

discharge at x (m^3 s^{-1}), L_f is the flow interval length (m), S_0 is the river bed slope, and p is the wetting perimeter (m).

4. Model Input

4.1. Atmospheric Forcing Data

[33] The atmospheric boundary conditions necessary to force the WEB-DHM comprise air temperature, relative humidity, air pressure, wind speed, downward longwave and shortwave radiation, as well as CO_2 and O_2 concentrations at a reference level within the atmospheric boundary layer. In practice, the mean value of O_2 concentration at one standard atmospheric pressure is defined as 20,900 Pa for current atmospheric conditions. The atmospheric CO_2 concentration is set to 36 Pa for this study.

4.2. Vegetation Parameters

[34] The vegetation static parameters used in the WEB-DHM, comprising morphological properties, optical properties, and physiological properties, are defined following the definitions provided by *Sellers et al.* [1996b]. The dynamic vegetation parameters are leaf area index (LAI) and the fraction of photosynthetically active radiation (FPAR) absorbed by the green vegetation canopy, which can be obtained from satellite data.

4.3. Soil Parameters

[35] The related soil static parameters for each soil texture class, including the saturated soil moisture content θ_s, the residual soil moisture content θ_r, the saturated hydrologic conductivity for soil surface $k_{surface}$, the van Genuchten parameters (α and n), and the hydraulic conductivity anisotropy ratio (anik), could be obtained from observation, literature or optimization. The anisotropic ratio (anik) is defined as [*Jackson*, 1992; *Cabral et al.*, 1992]

$$\text{anik} = K_{sp}/K_{sn} \geq 1, \quad (10)$$

where K_{sn} and K_{sp} are the saturated hydrological conductivities in the directions normal (n) and parallel (p) to the slope respectively (m s^{-1}). When the lateral subsurface flow and groundwater flow are being simulated, the lateral (p)

saturated hydraulic conductivity should be derived from the vertical saturated hydraulic conductivity (n) and anik.

5. Evaluation of the WEB-DHM in the Little Washita Basin

5.1. Data Sets for the Study Area

[36] The aim of this application is to test the performance of the WEB-DHM by comparing with various field observations having reliable accuracy. Although the model is developed for large-scale river basins, the evaluation is currently performed in a small region because of the limitation of filed observations.

[37] The Little Washita Basin, where stream flows are measured by USGS stream gauges while soil moisture and fluxes have been observed in SGP97 [*Jackson et al.*, 1999] and SGP99 [*Jackson and Hsu*, 2001] hydrology experiments, is suitable for validation of the coupled model. The Little Washita Basin is a subhumid river basin with an average annual rainfall of 750 mm. It has an area of 603 km^2, and the topography of the region is moderately rolling with a maximum relief less than 200 m (Figure 4). Land use is dominated by rangeland and pasture (63%) with significant areas of winter wheat and other crops concentrated in the floodplain and western parts of the basin. The land use types have been reclassified to SiB2 land use types for the study (see Figure 5). Soils include a wide range of textures with large regions of both coarse and fine textures (Figure 5). There are totally 42 Agricultural Research Service (ARS) Micronet stations distributed with 5 km spacing over the basin (Figure 4) and they provided the precipitation data for the study. Relative humidity, air temperature, and wind speed, as well as air pressure and solar radiation are obtained from three Oklahoma Mesonet stations (ACME, APAC, and NINN; see Figure 4), while the longwave radiation was estimated from the temperature, relative humidity, pressure, and solar radiation using the relationship between solar radiation and longwave radiation [*Crawford and Duchon*, 1999]. All the meteorological data, including precipitation and other surface meteorological data, were interpolated to a 500 m grid for the model simulations using the angular distance-weighted (ADW) interpolation method [*New et al.*, 2000].

[38] For SGP97, a high-resolution (30 m grid) normalized difference vegetation index (NDVI) map was acquired by the Landsat Thematic Mapper just after the SGP97 experiment was conducted (25 July 1997); whereas for SGP99, the NDVI map was acquired during the SGP99 experiment (15 July 1999). The LAI can be inferred from the NDVI by [*Yin and Williams*, 1997]

$$\text{LAI} = \text{LAI}_{\max}*(\text{NDVI} - \text{NDVI}_{\min})/(\text{NDVI}_{\max} - \text{NDVI}_{\min}). \quad (11)$$

Maximum and minimum NDVI values can be determined following *Sellers et al.* [1996b]. The FPAR is estimated using the expression [*Chang and Wetzel*, 1991]

$$\text{FPAR} = \begin{cases} 1.5*(\text{NDVI} - 0.1), & \text{NDVI} \leq 0.547 \\ 3.2*(\text{NDVI}) - 1.08, & \text{NDVI} > 0.547 \end{cases}. \quad (12)$$
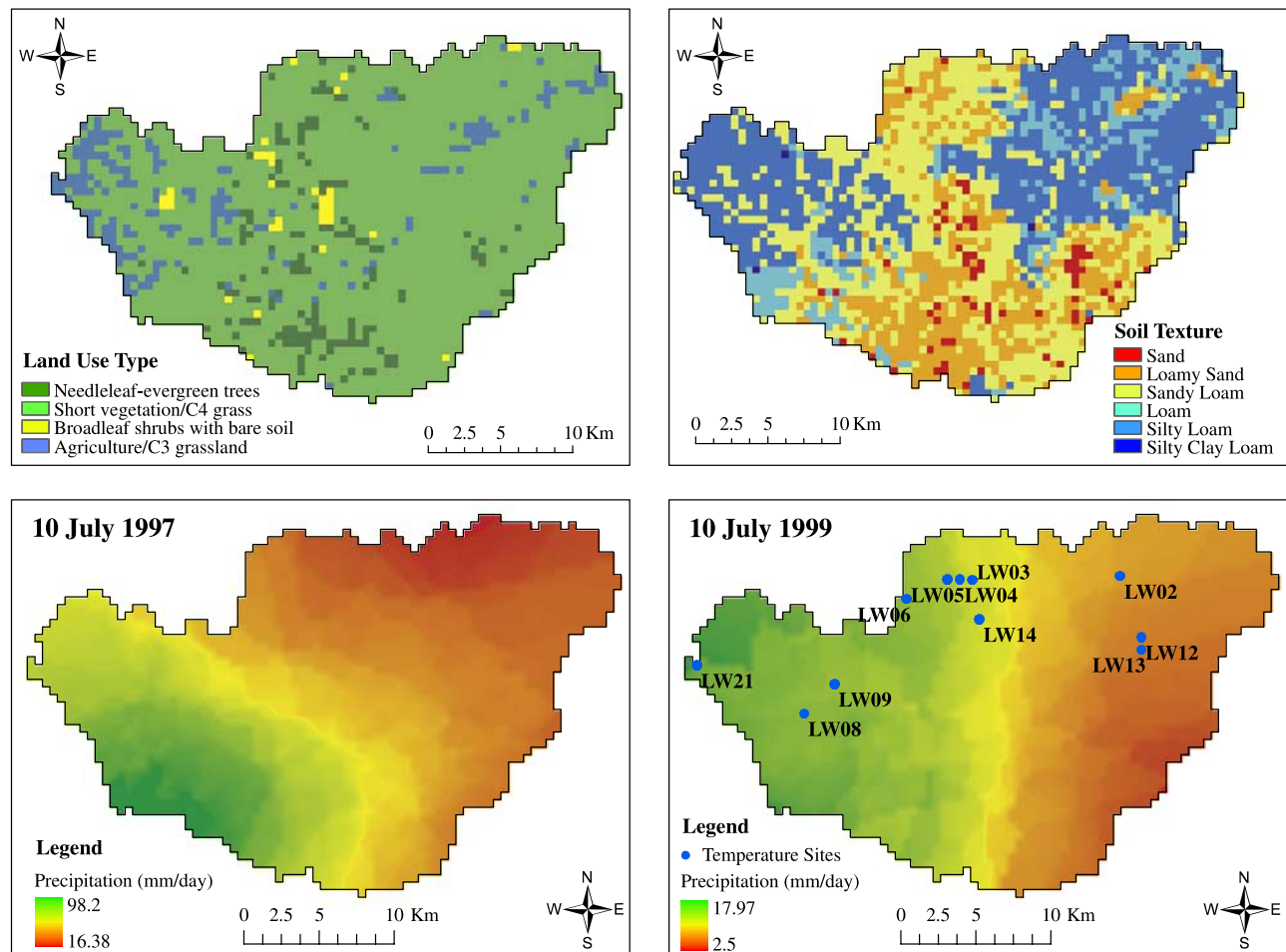
Figure 5. Spatial distribution of (top left) land use, (top right) soil texture, and daily precipitation for (bottom left) 10 July 1997 and (bottom right) 10 July 1999 (also showing the center for each temperature measuring field) in the Little Washita Basin.

[39] Observational data of soil properties, soil moisture, energy fluxes and CO_2 flux are available for the National Oceanic and Atmospheric Administration (NOAA) (LW02) flux site (Figure 4). At USGS stream gauge 07327550 (see Figure 4), discharge data have been obtained for model calibration and validation.

5.2. Model Calibration Using the SGP97 Data Sets

[40] In this section, the WEB-DHM is calibrated using the SGP97 observations. The simulations are performed in hourly time step and 500 m spatial resolution at both point scale and basin scale. At point scale, the parameters relating to the energy balance are calibrated by comparing observed and simulated energy components at the NOAA flux site. At basin scale, the hourly hydrograph for the USGS stream gauge 07327550 is calibrated by tuning soil hydraulic parameters.

[41] Surface soil moisture maps with a resolution of 800 m, derived by *Jackson et al.* [1999] from flights of the National Aeronautics and Space Administration P-3B aircraft fitted with the Electronically Scanned Thinned Array Radiometer (ESTAR) [*Le Vine et al.*, 1994], an L-band (1.413 GHz)

passive microwave sensor, are used for model initialization and verification.

5.2.1. Point Evaluation of the WEB-DHM at the NOAA (LW02) Flux Site

[42] The purpose of the simulation is to examine the vertical processes in the WEB-DHM. The observed soil moisture and temperature profiles (see Table 1) are used to initialize the model; while the initial water table depth is assumed as same as the initial depth of the unsaturated zone ($Ds = 1.15$ m).

[43] For the flux site, the LAI, FPAR, and green leaf fraction derived from the high-resolution (30 m grid) NDVI map, are 1.898, 0.27 and 0.974, respectively. The surface roughness length z_s is used to calculate the shear stress below the canopy. It is also related to the transfer efficiency of the sensible heat flux and the evaporative flux. Root depth D_r and surface roughness z_s are optimized as 0.75 m and 0.021 m, respectively. Other time-invariant vegetation parameters are set following *Sellers et al.* [1996b]. Soil properties have been kept equal to local field values derived from *Mohanty et al.* [2002].

[44] There were two versions of data set for the NOAA flux site submitted to the DAAC (http://daac.gsfc.nasa.gov/).

Table 1. Initial Conditions for the Flux Simulations at NOAA Site From 27 June to 19 July 1997 and Basin-Averaged Values of the Parameters Used in the Little Washita Basin

Symbol	Parameters	Unit	Value	Source
Initial Conditions for the Flux Simulations at NOAA Site				
T_c	Canopy temperature	K	297.1	*Jackson et al.* [1999]
T_g	Soil surface temperature	K	298.6	*Jackson et al.* [1999]
T_d	Deep soil temperature	K	294.8	*Jackson et al.* [1999]
θ_1	Volumetric soil moisture at $0.00 \sim 0.05$ m		0.254	*Jackson et al.* [1999]
θ_2	Volumetric soil moisture at $0.05 \sim 0.15$ m		0.270	*Jackson et al.* [1999]
θ_3	Volumetric soil moisture at $0.15 \sim 0.25$ m		0.353	*Jackson et al.* [1999]
θ_4	Volumetric soil moisture at $0.25 \sim 0.35$ m		0.375	*Jackson et al.* [1999]
θ_5	Volumetric soil moisture at $0.35 \sim 0.45$ m		0.329	*Jackson et al.* [1999]
θ_6	Volumetric soil moisture at $0.45 \sim 0.55$ m		0.382	*Jackson et al.* [1999]
θ_7	Volumetric soil moisture at $0.55 \sim 0.65$ m		0.388	*Jackson et al.* [1999]
θ_8	Volumetric soil moisture at $0.65 \sim 0.75$ m		0.401	*Jackson et al.* [1999]
θ_9	Volumetric soil moisture at $0.75 \sim 0.95$ m		0.382	*Jackson et al.* [1999]
θ_{10}	Volumetric soil moisture at $0.95 \sim 1.15$ m		0.380	*Jackson et al.* [1999]
Basin-Averaged Values of the Parameters				
θ_s	Saturated water content		0.47	*Mohanty et al.* [2002]
θ_r	Residual water content		0.06	*Mohanty et al.* [2002]
$k_{surface}$	Saturated hydraulic conductivity for soil surface	mm/h	25.8	Optimization
α	van Genuchten parameter		0.0348	Optimization
n	van Genuchten parameter		2.06	Optimization
anik	Hydraulic conductivity anisotropy ratio		15.2	Optimization
f	Hydraulic conductivity decay factor		1.36	Optimization
Mgw_{max}	Maximum surface water storage	m	0.02	Optimization
D_r	Root depth $(D_1 + D_2)$	m	0.75	Optimization
z_s	Surface roughness	m	0.021	Optimization
$NDVI_{max}$	NDVI at 98% of NDVI distribution		0.674	*Sellers et al.* [1996b]
$NDVI_{min}$	NDVI at 5% of NDVI distribution		0.039	*Sellers et al.* [1996b]

One data set is the original investigator's data set and the second data set is a modified version by the University of Wisconsin-Madison who quality-checked and modified the data with a "roving" EC system [*Jackson et al.*, 1999]. Modified eddy correlation (EC) flux data are used for model evaluation. The comparisons between observed and simulated hourly energy balance components and CO_2 fluxes at the NOAA flux site from 27 June to 19 July are shown in Figure 6 with bias error (BIAS) and root mean squared error (RMSE). The diurnal cycles of energy fluxes are well represented by the WEB-DHM with high accuracy. The BIAS for simulated net radiation (R_n), latent heat flux (LE), sensible heat flux (H), and ground heat flux (G) at the NOAA site are -4.1 W m^{-2}, 1.0 W m^{-2}, -0.6 W m^{-2}, and -5.0 W m^{-2}, while their RMSE values are 30.7 W m^{-2}, 36.8 W m^{-2}, 46.5 W m^{-2} and 38.2 W m^{-2}, respectively. It should be mentioned that there are totally 8 h during which H, LE, and CO_2 flux are not measured during the calibration period, and thus these hours are exempted in the comparisons.

[45] The measured surface CO_2 flux, arises as the net effect of the gross canopy photosynthesis (positive downward) and plant respiration and soil respiration (both positive upward). Figure 6 compares the simulated net CO_2 flux (plant respiration plus soil respiration minus gross canopy photosynthesis) and measurements. Results simulated by the model generally show good agreement with the observations with BIAS = -0.9 μ mol m^{-2}s^{-1} and RMSE = 4.6 μ mol m^{-2} s^{-1}, without tuning other parameters.

[46] The pixel-scale hourly evolutions of rainfall and surface soil moisture are illustrated in Figure 7. Diurnal cycles of soil moisture evaporation are well represented by the model, and reasonable responses of surface soil moisture to the rainfall events are reproduced.

[47] In general, the results at the NOAA flux site show the WEB-DHM is able to reproduce observed fluxes (water, energy and CO_2 fluxes) on a point scale, and the next step is application of the model to the whole Little Washita Basin for prediction of discharge and the spatial distribution of surface soil moisture.

5.2.2. Calibration of Discharge for the Period From 27 June to 19 July 1997

[48] The purpose of this simulation is to optimize soil water parameters to obtain good reproduction of the flood event that occurred during the SGP97 period. Furthermore, the optimized parameters can be used for flood prediction in 1999. In the discharge simulation, both BIAS and the Nash-Sutcliffe model efficiency coefficient (Nash) [*Nash and Sutcliffe*, 1970] are used for performance evaluation. Nash is defined as

$$\text{Nash} = 1 - \sum_{i=1}^{n} \left(Q_{oi} - Q_{si} \right)^2 \Big/ \sum_{i=1}^{n} \left(Q_{oi} - \overline{Q_o} \right)^2, \quad (13)$$

where Q_{oi} is observed discharge, Q_s is simulated discharge, n is the total number of time series for comparison, and $\overline{Q_o}$ is the mean value of observed discharge over the simulation period. The higher Nash is, the better a model performs. A perfect fit has Nash equal to one.
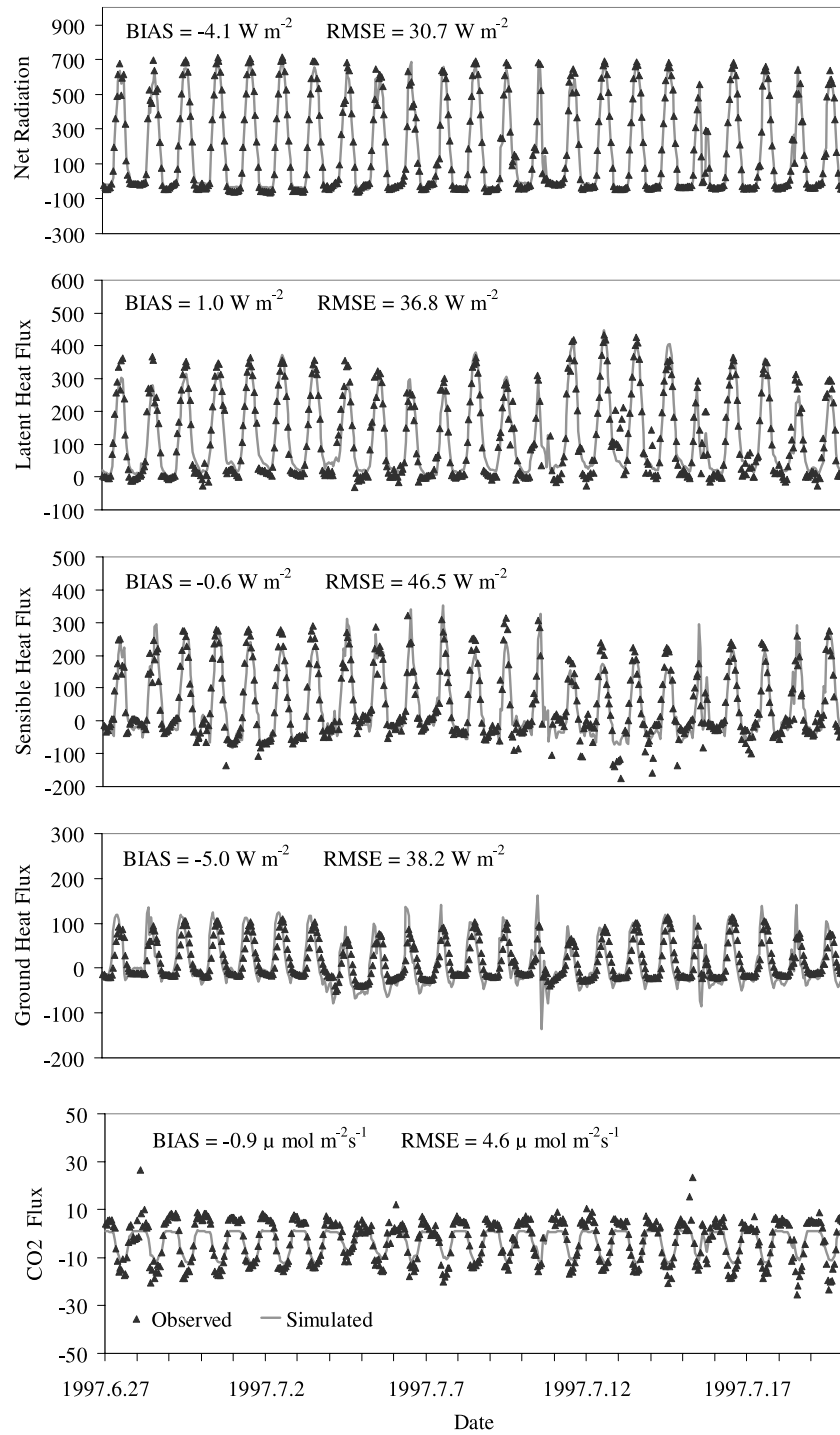
Figure 6. Observed and simulated energy balance components (unit: W m^{-2}) and CO$_2$ flux (unit: μ mol m^{-2}s^{-1}) at the NOAA flux site from 27 June to 19 July 1997.

[49] The initial soil moisture profile was obtained starting with a saturated profile and running the model several times using the meteorological forcing from 26 June to 16 July 1997 until the spatial-averaged surface soil moisture reached the same value as the ESTAR average.

[50] A trial and error method is used to optimize several parameters by matching the simulated and observed flood peaks and tails: the saturated hydraulic conductivity for soil surface $k_{surface}$, the van Genuchten parameters (α and n), the hydraulic conductivity anisotropy ratio (anik), the hydraulic conductivity decay factor (f), and the maximum surface water storage (Mgw_{max}). These soil hydraulic parameters are assigned for each soil texture class, and thus spatially distributed in accordance with the soil texture classes. The basin-averaged values of the optimized parameters are listed in Table 1.
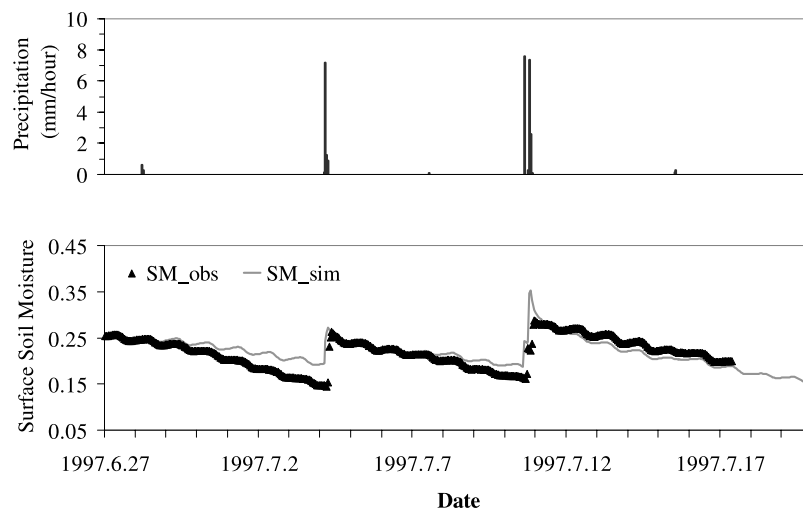
Figure 7. Precipitation and surface (top 5 cm) soil moisture at the NOAA flux site from 27 June to 19 July 1997.

[51] The calibrated hydrograph and accumulated discharge are shown in Figure 8. It is shown that after calibration, the model can reproduce both the peak flow and base flow very well with Nash equal to 0.956 and BIAS equal to −0.6%. In addition, the simulated accumulated discharge agrees well with the observed accumulated discharge and this confirms the model is capable of accurately simulating the basin-averaged water budget.

5.2.3. Surface Soil Moisture Evolution

[52] The soil moisture distribution derived from the ESTAR data by *Jackson et al.* [1999] are used to test the model's ability to predict the basin-scale surface soil moisture evolution.

[53] The comparison of the basin-averaged surface (top 5 cm) soil moisture between the model simulation and ESTAR estimates is presented in Figure 8 (bottom). After the calibration for streamflow at the USGS stream gauge 07327550, simulated basin-averaged soil moisture agrees fairly well with ESTAR estimates.

[54] Figure 9 illustrates the spatial distributions of simulated surface soil moisture compared with ESTAR estimates during the SGP97 period. In general, the surface soil moisture patterns simulated by the WEB-DHM appear similar to ESTAR estimates. The major rainfall event during the calibration period occurred on 10 July 1997. By comparing the maps in Figure 5 (soil texture map and daily precipitation map for 10 July 1997) with the soil moisture maps in Figure 9, some conclusions can be drawn. First, in the dry periods (3 July and 16 July), the spatial patterns of surface soil moisture are mainly controlled by the soil texture, which controls the infiltration and soil moisture transport in the soil through inferred hydraulic conductivity. Second, the surface soil moisture patterns are strongly determined by the precipitation distribution just after the rainfall event (11 July), especially for the first several hours. Third, within the recession period (see 12–13 July), the soil texture pattern becomes evident in the soil moisture map, while the influence of precipitation sharply declines with soil drainage.
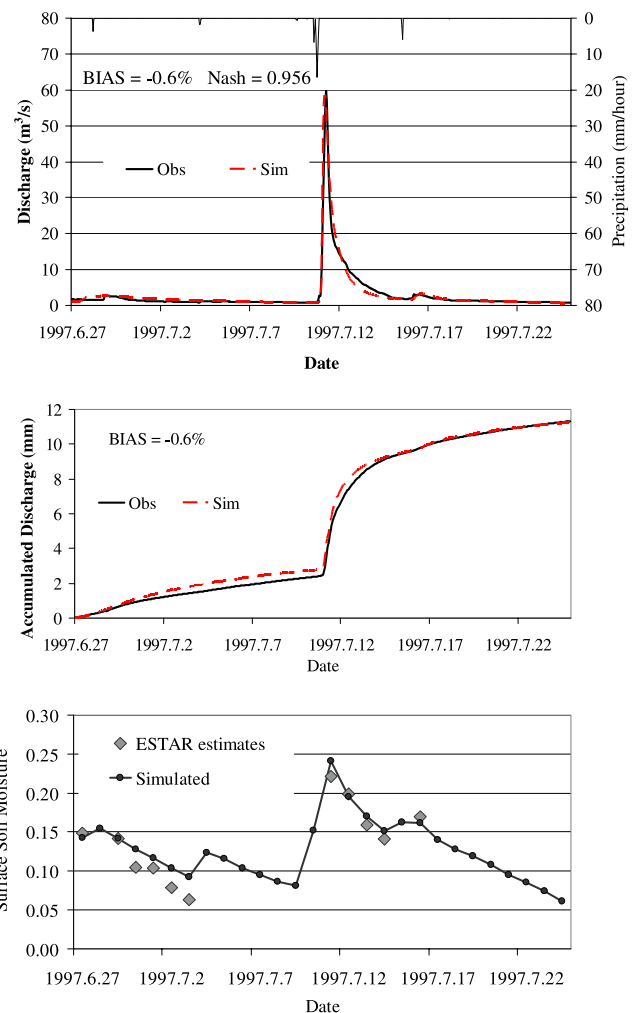

Figure 8. Hourly (top) hydrograph and (middle) accumulated discharge at the USGS stream gauge 07327550, as well as (bottom) basin-averaged surface soil moisture evolution by model simulation and ESTAR estimates from 27 June to 24 July 1997.
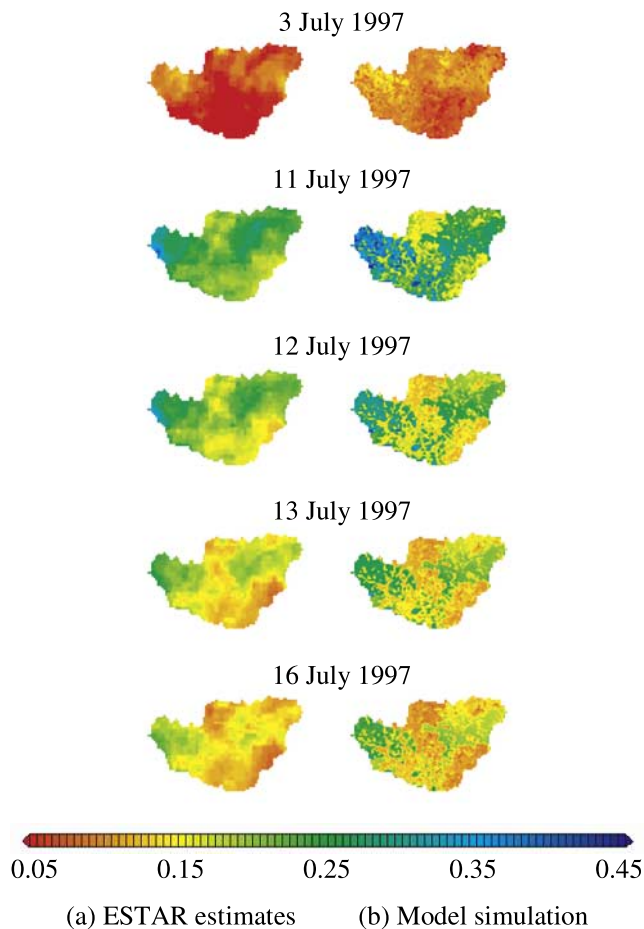
Figure 9. Comparisons of spatial patterns of surface soil moisture between (a) ESTAR estimates and (b) model simulation during the period from 27 June to 17 July 1997.

5.3. Model Validation Using the SGP99 Data Sets and Daily Discharge

[55] By keeping the calibrated parameters constant, the WEB-DHM is validated using the SGP99 observations and USGS discharges. The model was run many times with the same meteorological forcing from 1 September 1998 to 31 August 1999 until a hydrological equilibrium was reached. The results from the last run are analyzed.

[56] The model validations are performed at both point scale and basin scale. At point scale, the simulated soil surface temperatures in the 11 model grids are compared with observed values measured using handheld infrared thermometers at 11 temperature measuring sites (see Figure 5, bottom right) from 8 to 20 July 1999. At basin scale, the model is validated in the prediction of the annual largest flood peak in 1999 at the USGS stream gauge 07327550 and prediction of the spatial surface soil moisture in the SGP99 period with a lead time of several months.

[57] In the validation period, the surface soil moisture maps (800 m grid) derived by *Jackson et al.* [2002] from aircraft measurements using the NOAA Polarimetric Scanning Radiometer (PSR) C-band scanhead [*Piepmeier and Gasiewski*, 2001] are used for model validation. The PSR measurements mimic Advanced Microwave Scanning Radiometer (AMSR) measurements with respect to the frequency

and viewing angle. The PSR C-band radiometer was flown for the first time as part of SGP99 for the development and validation of soil moisture retrieval algorithms for the AMSR, which holds great promise for soil moisture mapping in regions of low vegetation [*Njoku et al.*, 2000]. *Jackson et al.* [2002] revealed that for vegetation conditions typical of the SGP99 region, the quality of the C-band derived soil moisture is comparable to the corresponding L-band product (ESTAR) during the SGP99 study period.

5.3.1. Soil Surface Temperature

[58] The surface temperature data collected using handheld infrared thermometers in SGP99 are used for model verification. Information from Little Washita fields (LW) 2–9, 12–14, and 21 have been collected, and LW 7 is excluded from the comparison since it is outside the delineated watershed of this study. The temperature sampling was intended to estimate the field average and thus a rectangular grid was set up for each field. For almost all fields there are no measurements for 10 July, for it rained on this day. All temperature measurements at a field were taken within 3 h of each other from day to day and all temperatures are measured in degrees Celsius. Figure 5 (bottom right) shows the central locations of all 11 measuring fields. During the basin-scale simulation from 1 September 1998 to 31 August 1999, the model was initialized by soil surface temperature observations on 8 July for all the fields except LW 9, for which observations on 9 July were used.

[59] The comparison between simulations and observations are given Figure 10. For the individual fields, the simulated surface temperatures generally have the same trend as the average surface temperature of all fields has. Small discrepancies exist on several days for all 11 sites. The all-field average surface temperature obtained from the model simulation agrees fairly well with the average of measurements. All sites show a sharp decrease from 9 to 10 July due to a rainfall event on 10 July covering the whole Little Washita basin (see Figure 5). From 10 to 20 July, the surface temperatures for all sites generally have the same increasing trend.

5.3.2. Annual Largest Flood Peak Simulation

[60] Figure 11 (top) illustrates the daily observed and simulated streamflows at USGS gauge 07327500 for the whole hydroyear from 1 September 1998 to 31 August 1999. Therefore, this simulation covers the annual largest flood in 1999 and also the SGP99 period. Using the same precipitation data from the 42 ARS Micronet stations, the results with acceptable accuracies were obtained with a Nash value of 0.715 and BIAS value of 25.3%. Though the magnitude of the annual largest flood peak was slightly overestimated, the peak time was accurately predicted. Generally, the base flows agree well with observed values except overestimates in the recession periods.

5.3.3. Soil Moisture Evolution

[61] The soil moisture distribution derived from the PSR C-band data by *Jackson et al.* [2002] is used to further validate the model's capability to predict basin-scale surface soil moisture evolution with a long lead time (e.g., several months).

[62] A comparison of the basin-averaged surface (top 5 cm) soil moisture between the model simulation and PSR C-band estimates is presented in Figure 11 (middle and bottom). The simulated basin-averaged soil moisture agrees well with
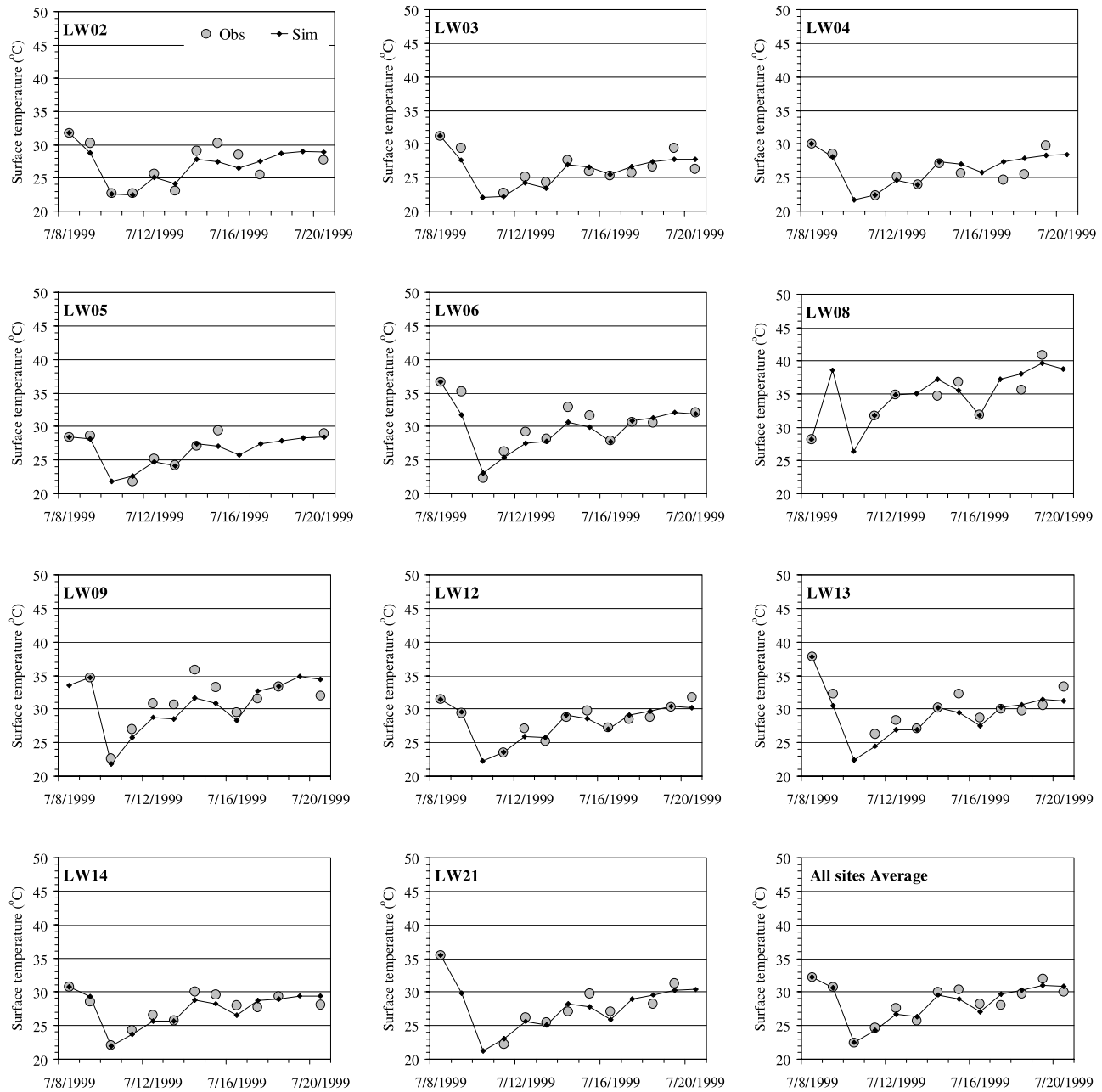
Figure 10. Comparison of the surface soil temperature between the model simulation and observation by handheld infrared thermometers at 11 sites from 8 to 20 July 1999.

PSR C-band estimates in terms of the general trend, except for the obvious overestimations on some dry days (8−9 and 14−15 July). This is not surprising since the vertical resolution of PSR C-band data depends on the penetration depth of C-band radiation, which is a function of soil moisture [*Drusch et al.*, 2004]. Since penetration depth increases for dry soils, the depth of the observed soil layer should vary between ∼0.5 and ∼3 cm [*Ulaby et al.*, 1982]. The topsoil layer in the WEB-DHM has a depth of 5 cm. During dry-down events (e.g., 8−9 and 14−15 July), water infiltrates into deeper layers and evaporates from the surface layer. Consequently, the 5-cm simulation will contain more water than the C-band estimate, although the penetration depth of C-band radiation increases.

[63] Figure 12 illustrates the spatial distributions of simulated surface soil moisture compared with PSR C-band estimates during the SGP99 period. The surface soil moisture patterns obtained by model simulation are also very similar to PSR C-band estimates. The major rainfall event during the SGP99 period occurred on 10 July 1999. By comparing the maps in Figure 5 (soil texture map and daily precipitation map for 10 July 1999) with the soil moisture maps in Figure 12, we can confirm our conclusions drawn from SGP97 that soil moisture maps are mainly determined by the coaction of precipitation and soil texture. On 11 July, just after a small rainfall event, the precipitation pattern is evident in the soil moisture map derived from PSR C-band data and the simulated soil moisture map. With time
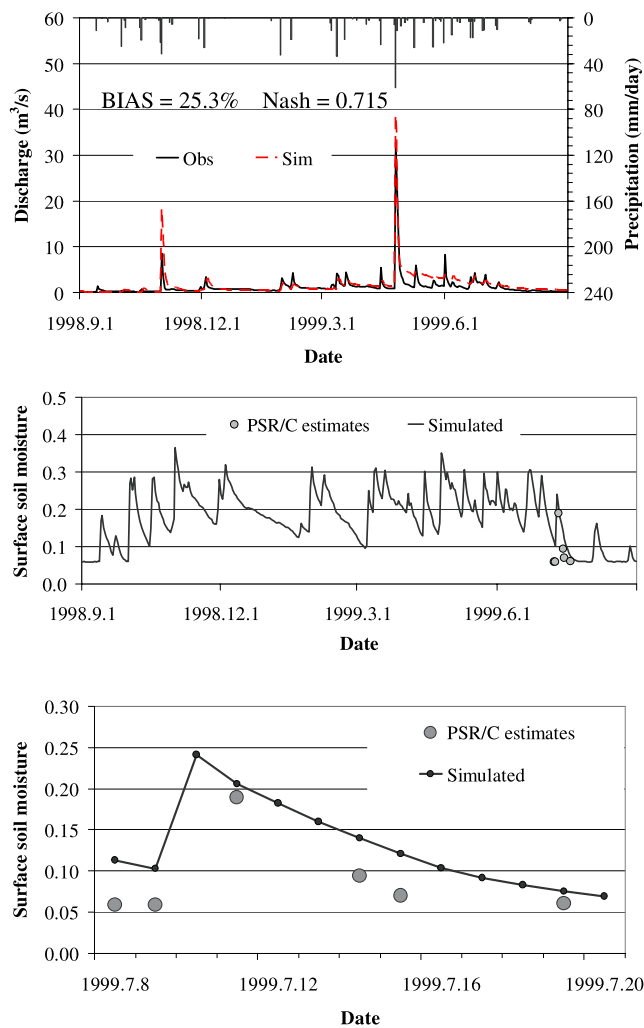
Figure 11. (top) Daily hydrograph at the USGS stream gauge 07327550 and (middle) daily evolution of basin-averaged surface soil moisture from model simulation compared with PSR C-band estimates and (bottom) an enlargement showing the SGP99 period from 1 September 1998 to 31 August 1999.

passing, soil texture exerted more influence on the determination of the soil moisture spatial distribution.

6. Concluding Remarks

[64] In this study, a new biosphere hydrological model, the WEB-DHM, has been developed by coupling a realistic LSM (SiB2) with a geomorphology-based DHM (GBHM). This paper described the formulation of the WEB-DHM and its evaluation when applied to the Little Washita Basin using various field observations obtained from SGP97 and SGP99. The model demonstrated the ability to reproduce point-scale energy fluxes (RMSE < 50 W m^{-2}) as well as CO_2 flux (RMSE = 4.6 μ mol m^{-2} s^{-1}), the ability to predict discharges (both peak and base flows) at the stream gauge with Nash equal to 0.956 for the calibration period and 0.715 for the validation period, and the ability to predict the basin-scale surface soil moisture evolution in a spatially distributed manner. To our knowledge, this work is the first to have undertaken the development and evaluation of a

distributed biosphere hydrological model by using such comprehensive field observations, which include not only discharge but also energy and CO_2 flux observations, as well as spatial surface soil moisture and multiple-site surface temperature observations.

[65] As a distributed biosphere hydrological model, the WEB-DHM incorporating SiB2 uses a realistic canopy photosynthesis-conductance model to describe the simultaneous transfer of CO_2 and water vapor into and out of the vegetation respectively for each model grid. In this model, photosynthesis and conductance are explicitly connected. The basis for the leaf photosynthesis-conductance model used in the WEB-DHM are the C_3 photosynthesis model of *Farquhar et al.* [1980], as expanded on by *Collatz et al.* [1991] and others, the C_4 model of *Collatz et al.* [1992], and the stomatal model of *Ball* [1988]. Details can be found in Appendix C of *Sellers et al.* [1996a]. The improvement makes the WEB-DHM capable of continuously simulating the exchanges of CO_2 besides water and energy during land-atmosphere interactions in the SVAT system, at the basin scale in a spatially distributed manner. In future studies, the WEB-DHM can be coupled with mesoscale atmospheric models or GCMs for improved predictions of fluxes and streamflows from regional to global scales, since it has explicitly addressed the groundwater dynamics and the topographically driven lateral water redistributions.

[66] Furthermore, in a hydrological simulation, parameters (such as soil porosity, and surface roughness parameters)
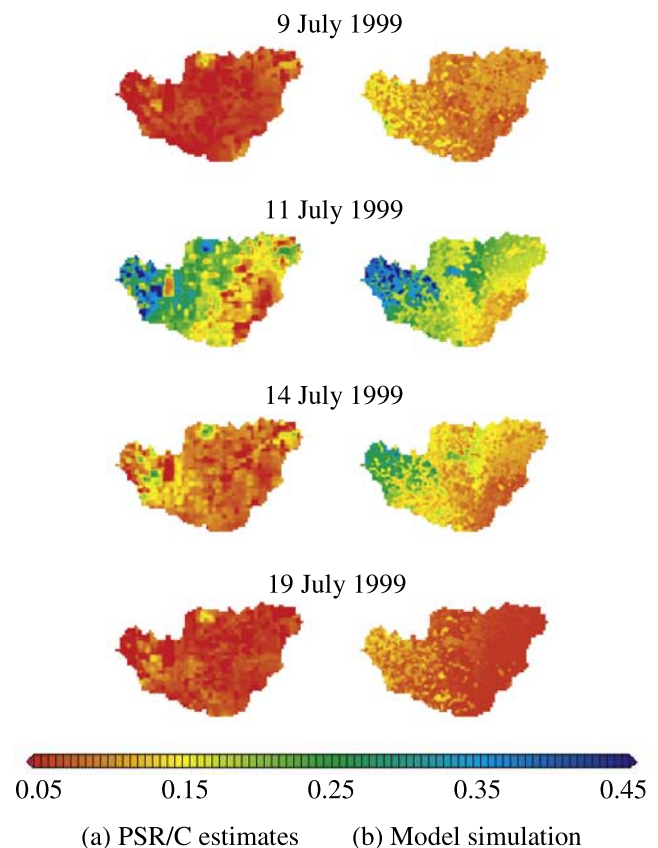

(a) PSR/C estimates   (b) Model simulation

Figure 12. Comparison of the spatial pattern of surface soil moisture between (a) PSR C-band estimates and (b) model simulation during the period from 8 to 20 July 1999.

and initial conditions (e.g., surface soil moisture) are crucial to the model's performance in the prediction of floods and surface soil wetness. However, they are usually not measured in large-scale river basins, especially in ungauged basins. Therefore, land data assimilation systems are expected to obtain more reliable parameter and near-surface soil moisture data for the WEB-DHM by merging information from satellites, ground-based stations, and models [*Yang et al.*, 2007]. Advances in this aspect would contribute to the initialization and parameterization of the model, improving the capability of hazard (flood and drought) predictions under climate changes.

References

Abbott, M. B., J. C. Bathurst, J. A. Cunge, P. E. O'Connell, and J. Rasmussen (1986), An introduction to the European hydrological system—Systeme Hydrologique Europeen, SHE, 2. Structure of a physically based distributed modeling system, *J. Hydrol.*, 87, 61–77, doi:10.1016/0022-1694(86)90115-0.

Avissar, R., C. P. Weaver, D. Werth, R. A. Pielke Sr., R. Rabin, A. J. Pitman, and M. A. Silva Dias (2004), The regional climate, in *Vegetation, Water, Humans, and the Climate: A New Perspective on an Interactive System*, edited by P. Kabat et al., pp. 21–32, Springer, New York.

Ball, J. T. (1988), An analysis of stomatal conductance, Ph.D. thesis, 89 pp., Stanford Univ., Stanford, Calif.

Bathurst, J. C., J. M. Wicks, and P. E. O'Connell (1995), The SHE/SHESED basin scale water flow and sediment transport modeling system, in *Computer Models of Watershed Hydrology*, edited by V. P. Singh, pp. 563–594, Water Resour. Publ., Highlands Ranch, Colo.

Bertoldi, G., R. Rigon, and T. M. Over (2006), Impact of watershed geomorphic characteristics on the energy and water budgets, *J. Hydrometeorol.*, 7, 389–403.

Braun, F. J., and G. Schadler (2005), Comparison of soil hydraulic parameterizations for mesoscale meteorological models, *J. Appl. Meteorol.*, 44, 1116–1132, doi:10.1175/JAM2259.1.

Cabral, M. L. G., R. Bras, and D. Entekhabi (1992), A kinematic model of infiltration and runoff generation in layered and sloped soils, *Adv. Water Resour.*, 15, 311–324, doi:10.1016/0309-1708(92)90017-V.

Campbell, G. S. (1974), Simple method for determining unsaturated conductivity from moisture retention data, *Soil Sci.*, 117, 311–314, doi:10.1097/00010694-197406000-00001.

Chang, J. T., and P. J. Wetzel (1991), Effects of spatial variation of soil moisture and vegetation on the evolution of a prestorm environment: A numerical case study, *Mon. Weather Rev.*, 119, 1368–1390, doi:10.1175/1520-0493(1991)119<1368:EOSVOS>2.0.CO;2.

Chen, F., and R. Avissar (1994), The impact of land-surface wetness heterogeneity on mesoscale heat fluxes, *J. Appl. Meteorol.*, 33, 1323–1340, doi:10.1175/1520-0450(1994)033<1323:TIOLSW>2.0.CO;2.

Clapp, R. B., and G. M. Hornberger (1978), Empirical equations for some soil hydraulic properties, *Water Resour. Res.*, 14, 601–604, doi:10.1029/WR014i004p00601.

Collatz, G. J., J. T. Ball, C. Grivet, and J. A. Berry (1991), Physiological and environmental regulation of stomatal conductance, photosynthesis and transpiration: A model that includes a laminar boundary layer, *Agric. For. Meteorol.*, 54, 107–136, doi:10.1016/0168-1923(91)90002-8.

Collatz, G. J., M. Ribas-Carbo, and J. A. Berry (1992), Coupled photosynthesis-stomatal conductance model for leaves of C_4 plants, *Aust. J. Plant Physiol.*, 19, 519–538.

Crawford, T. M., and C. E. Duchon (1999), An improved parameterization for estimating effective atmospheric emissivity for use in calculating daytime downwelling longwave radiation, *J. Appl. Meteorol.*, 38, 474–480, doi:10.1175/1520-0450(1999)038<0474:AIPFEE>2.0.CO;2.

Dai, Y., et al. (2003), The Common Land Model, *Bull. Am. Meteorol. Soc.*, 84, 1013–1023, doi:10.1175/BAMS-84-8-1013.

Dickinson, R. E., A. Henderson-Sellers, P. J. Kennedy, and M. F. Wilson (1986), Biosphere-atmosphere transfer scheme (BATS) for the NCAR community climate model, *NCAR Tech. Note*, TN-275+STR, 69 pp., Natl. Cent. for Atmos. Res., Boulder, Colo.

Dickinson, R. E., M. Shaikh, R. Bryant, and L. Graumlich (1998), Interactive canopies for a climate model, *J. Clim.*, 11, 2823–2836, doi:10.1175/1520-0442(1998)011<2823:ICFACM>2.0.CO;2.

Drusch, M., E. F. Wood, H. Gao, and A. Thiele (2004), Soil moisture retrieval during the Southern Great Plains Hydrology Experiment 1999: A comparison between experimental remote sensing data and operational products, *Water Resour. Res.*, 40, W02504, doi:10.1029/2003WR002441.

Farquhar, G. D., S. V. Caemmerer, and J. A. Berry (1980), A biochemical model of photosynthetic CO_2 assimilation in leaves of C_3 species, *Planta*, 149, 78–90, doi:10.1007/BF00386231.

Fast, J. D., and M. D. McCorcle (1991), The effect of heterogeneous soil moisture on a summer baroclinic circulation in the central United States, *Mon. Weather Rev.*, 119, 2140–2167, doi:10.1175/1520-0493(1991)119<2140:TEOHSM>2.0.CO;2.

Findell, K. L., and E. A. B. Eltahir (2003), Atmospheric controls on soil moisture-boundary layer interactions, Part 1: Framework development, *J. Hydrometeorol.*, 4, 552–569, doi:10.1175/1525-7541(2003)004<0552:ACOSML>2.0.CO;2.

Freeze, R. A., and R. L. Harlan (1969), Blueprint for a physically based digitally simulated hydrological response model, *J. Hydrol.*, 9, 237–258, doi:10.1016/0022-1694(69)90020-1.

Henderson-Sellers, A., Z. Yang, and R. E. Dickinson (1993), The project for intercomparison of land surface parameterization schemes, *Bull. Am. Meteorol. Soc.*, 74, 1335–1349, doi:10.1175/1520-0477(1993)074<1335:TPFIOL>2.0.CO;2.

Hutjes, R. W. A., et al. (1998), Biospheric aspects of the hydrological cycle-Preface, *J. Hydrol.*, 212–213, 1–21, doi:10.1016/S0022-1694(98)00255-8.

Intergovernmental Panel on Climate Change (2007), *Climate Change 2007: Climate Change Impacts, Adaptation and Vulnerability, Summary for Policymakers*, World Meteorol. Org., Geneva.

Ivanov, V. Y., E. R. Vivoni, R. L. Bras, and D. Entekhabi (2004), Catchment hydrologic response with a fully distributed triangulated irregular network model, *Water Resour. Res.*, 40, W11102, doi:10.1029/2004WR003218.

Jackson, C. (1992), Hillslope infiltration and lateral downslope unsaturated flow, *Water Resour. Res.*, 28(9), 2533–2539, doi:10.1029/92WR00664.

Jackson, T. J., and A. Y. Hsu (2001), Soil moisture and TRMM microwave imager relationships in the Southern Great Plains 1999 (SGP99) Experiment, *IEEE Trans. Geosci. Remote Sens.*, 39, 1632–1642, doi:10.1109/36.942541.

Jackson, T. J., D. M. Le Vine, A. Y. Hsu, A. Oldak, P. J. Starks, C. T. Swift, J. D. Isham, and M. Haken (1999), Soil moisture mapping at regional scales using microwave radiometry: The Southern Great Plains Hydrology Experiment, *IEEE Trans. Geosci. Remote Sens.*, 37, 2136–2151, doi:10.1109/36.789610.

Jackson, T. J., A. Gasiewski, A. Oldak, M. Klein, E. G. Njoku, A. Yevgrafov, S. Christiani, and R. Bindlish (2002), Soil moisture retrieval using the C-band polarimetric scanning radiometer during the Southern Great Plains 1999 Experiment, *IEEE Trans. Geosci. Remote Sens.*, 40, 2151–2161, doi:10.1109/TGRS.2002.802480.

Koster, R. D., and P. C. D. Milly (1997), The interplay between transpiration and runoff formulations in land surface schemes used with atmospheric models, *J. Clim.*, 10, 1578–1591, doi:10.1175/1520-0442(1997)010<1578:TIBTAR>2.0.CO;2.

Leese, J., T. Jackson, A. Pitman, and P. Dirmeyer (2001), Meeting summary: GEWEX/BAHC international workshop on soil moisture monitoring, analysis, and prediction for hydrometeorological and hydroclimatological applications, *Bull. Am. Meteorol. Soc.*, 82, 1423–1430.

Le Vine, D. M., A. J. Griffis, C. T. Swift, and T. J. Jackson (1994), ESTAR: A synthetic aperture microwave radiometer for remote sensing applications, *Proc. IEEE*, 82(12), 1787–1801, doi:10.1109/5.338071.

Li, B., and R. Avissar (1994), The impact of spatial variability of land-surface characteristics on land-surface heat fluxes, *J. Clim.*, 7, 527–537, doi:10.1175/1520-0442(1994)007<0527:TIOSVO>2.0.CO;2.

Liang, X., D. P. Lettenmaier, E. F. Wood, and S. J. Burges (1994), A simple hydrologically based model of land surface water and energy fluxes for general circulation models, *J. Geophys. Res.*, 99, 14,415–14,428, doi:10.1029/94JD00483.

Manabe, S. (1969), Climate and ocean circulation: 1. Atmospheric circulation and circulation and hydrology of Earth's surface, *Mon. Weather Rev.*, 97, 739–774, doi:10.1175/1520-0493(1969)097<0739:CATOC>2.3.CO;2.

Maxwell, R. M., F. K. Chow, and S. J. Kollet (2007), The groundwater-land-surface-atmosphere connection: Soil moisture effects on the atmospheric boundary layer in fully coupled simulations, *Adv. Water Resour.*, 30, 2447–2466, doi:10.1016/j.advwatres.2007.05.018.

Mengelkamp, H. T., K. Warrach, and E. Raschke (1999), SEWAB—A parameterization of the surface energy and water balance for atmospheric

and hydrologic models, *Adv. Water Resour.*, 23, 165–175, doi:10.1016/S0309-1708(99)00020-2.

Milly, P. C. D. (1992), Potential evaporation and soil moisture in general circulation models, *J. Clim.*, 5, 209–226, doi:10.1175/1520-0442(1992)005<0209:PEASMI>2.0.CO;2.

Mohanty, B. P., P. J. Shouse, D. A. Miller, and M. T. van Genuchten (2002), Soil property database: Southern Great Plains 1997 Hydrology Experiment, *Water Resour. Res.*, 38(5), 1047, doi:10.1029/2000WR000076.

Nash, J. E., and J. V. Sutcliffe (1970), River flow forecasting through conceptual models part I—A discussion of principles, *J. Hydrol.*, 10, 282–290, doi:10.1016/0022-1694(70)90255-6.

New, M., M. Hulme, and P. Jones (2000), Representing twentieth-century space-time climate variability. Part II: Development of 1901-96 monthly grids of terrestrial surface climate, *J. Clim.*, 13, 2217–2238, doi:10.1175/1520-0442(2000)013<2217:RTCSTC>2.0.CO;2.

Njoku, E. G., T. Koike, T. J. Jackson, and S. Paloscia (2000), Retrieval of soil moisture from AMSR data, in *Microwave Radiometry and Remote Sensing of the Earth's Surface and Atmosphere*, edited by P. Pampaloni and S. Paloscia, pp. 525–533, VSP Publ., Utrecht, Netherlands.

O'Callaghan, J. F., and D. M. Mark (1984), The extraction of drainage networks from digital elevation data, *Comput. Vision Graphics Image Process.*, 28, 328–344.

Pielke, R. A., Sr. (2001), Influence of the spatial distribution of vegetation and soils on the prediction of cumulus convective rainfall, *Rev. Geophys.*, 39, 151–177, doi:10.1029/1999RG000072.

Piepmeier, J. R., and A. J. Gasiewski (2001), High-resolution passive microwave polarimetric mapping of ocean surface wind vector fields, *IEEE Trans. Geosci. Remote Sens.*, 39, 606–622, doi:10.1109/36.911118.

Pietroniro, A., and E. D. Soulis (2003), A hydrology modeling framework for the Mackenzie GEWEX programme, *Hydrol. Processes*, 17, 673–676, doi:10.1002/hyp.5104.

Rawls, W. J., and D. L. Brakensiek (1982), Estimating soil water retention from soil properties, *J. Irrig. Drain. Div. Am. Soc. Civ. Eng.*, 108, 166–171.

Rigon, R., G. Bertoldi, and T. M. Over (2006), GEOtop: A distributed hydrological model with coupled water and energy budgets, *J. Hydrometeorol.*, 7, 371–388.

Robinson, J., and M. Sivapalan (1996), Instantaneous response functions of overland flow and subsurface stormflow for catchment models, *Hydrol. Processes*, 10, 845–862, doi:10.1002/(SICI)1099-1085(199606)10:6<845::AID-HYP375>3.0.CO;2-7.

Sellers, P. J., Y. Mintz, Y. C. Sud, and A. Dalcher (1986), A simple biosphere model (SiB) for use within general circulation models, *J. Atmos. Sci.*, 43(6), 505–531, doi:10.1175/1520-0469(1986)043<0505:ASBMFU>2.0.CO;2.

Sellers, P. J., D. A. Randall, G. J. Collatz, J. A. Berry, C. B. Field, D. A. Dazlich, C. Zhang, G. D. Collelo, and L. Bounoua (1996a), A revised land surface parameterization (SiB2) for atmospheric GCMs, Part I: Model formulation, *J. Clim.*, 9, 676–705, doi:10.1175/1520-0442(1996)009<0676:ARLSPF>2.0.CO;2.

Sellers, P. J., S. O. Los, C. J. Tucker, C. O. Justice, D. A. Dazlich, G. J. Collatz, and D. A. Randall (1996b), A revised land surface parameterization (SiB2) for atmospheric GCMs, Part II: The generation of global fields of terrestrial biophysical parameters from satellite data, *J. Clim.*, 9, 706–737, doi:10.1175/1520-0442(1996)009<0706:ARLSPF>2.0.CO;2.

Tang, Q., T. Oki, and S. Kanae (2006), A distributed biosphere hydrological model (DBHM) for large river basin, *Annu. J. Hydraul. Eng.*, 50, 37–42.

Tang, Q., T. Oki, S. Kanae, and H. Hu (2007), The influence of precipitation variability and partial irrigation within grid cells on a hydrological simulation, *J. Hydrometeorol.*, 8, 499–512, doi:10.1175/JHM589.1.

Tang, Q., T. Oki, S. Kanae, and H. Hu (2008), Hydrological cycles change in the Yellow River basin during the last half of the 20th century, *J. Clim.*, 21, 1790–1806, doi:10.1175/2007JCLI1854.1.

Tarboton, D. G., R. L. Bras, and I. Rodriguez-Iturbe (1991), On the extraction of channel networks from digital elevation data, *Hydrol. Processes*, 5, 81–100, doi:10.1002/hyp.3360050107.

Ulaby, R. T., R. K. Moore, and A. K. Fung (1982), *Radar Remote Sensing and Surface Scattering and Emission Theory*, vol. II, 1064 pp., Artech House, Norwood, Mass.

van Genuchten, M. T. (1980), A closed form equation for predicting the hydraulic conductivity of unsaturated soils, *Soil Sci. Soc. Am. J.*, 44, 892–898.

Verdin, K. L., and J. P. Verdin (1999), A topological system for delineation and codification of the Earth's river basins, *J. Hydrol.*, 218, 1–12, doi:10.1016/S0022-1694(99)00011-6.

Verseghy, D. L. (1991), CLASS—A Canadian Land Surface Scheme for GCMs. 1. Soil model, *Int. J. Climatol.*, 11, 111–133.

Wang, L. (2007), Development of a distributed runoff model coupled with a land surface scheme, Ph.D. thesis, Univ. of Tokyo, Tokyo.

Wang, L., Z. Wang, H. Yin, D. Yang, and S. He (2006), A distributed hydrological model—GBHM and its application in a middle-scale catchment (in Chinese), *J. Glaciol. Geocryol.*, 28(2), 256–261.

Yang, D. (1998), Distributed hydrological model using hillslope discretization based on catchment area function: Development and applications, Ph.D. thesis, Univ. of Tokyo, Tokyo.

Yang, D., S. Herath, and K. Musiake (2000), Comparison of different distributed hydrological models for characterization of catchment spatial variability, *Hydrol. Processes*, 14, 403–416, doi:10.1002/(SICI)1099-1085(20000228)14:3<403::AID-HYP945>3.0.CO;2-3.

Yang, D., T. Koike, and H. Tanizawa (2004), Application of a distributed hydrological model and weather radar observations for flood management in the upper Tone River of Japan, *Hydrol. Processes*, 18, 3119–3132, doi:10.1002/hyp.5752.

Yang, K., T. Watanabe, T. Koike, X. Li, H. Fujii, K. Tamagawa, Y. Ma, and H. Ishikawa (2007), Auto-calibration system developed to assimilate AMSR-E data into a land surface model for estimating soil moisture and the surface energy budget, *J. Meteorol. Soc. Jpn.*, 85A, 229–242, doi:10.2151/jmsj.85A.229.

Yeh, P. J. F., and E. A. B. Eltahir (2005), Representation of water table dynamics in a land surface scheme. Part I: Model development, *J. Clim.*, 18, 1861–1880, doi:10.1175/JCLI3330.1.

Yin, Z., and T. H. L. Williams (1997), Obtaining spatial and temporal vegetation data from Landsat MSS and AVHRR/NOAA satellite images for a hydrologic model, *Photogramm. Eng. Remote Sens.*, 63(1), 69–77.

Yu, Z., D. Pollard, and L. Cheng (2006), On continental-scale hydrologic simulations with a coupled hydrologic model, *J. Hydrol.*, 331, 110–124, doi:10.1016/j.jhydrol.2006.05.021.

————————————

R. Bindlish and T. J. Jackson, Hydrology and Remote Sensing Laboratory, ARS, USDA, Beltsville, MD 20705, USA.

T. Koike and L. Wang, Department of Civil Engineering, University of Tokyo, Hongo 7-3-1, Bunkyo-ku, Tokyo 113-8656, Japan. (wang@hydra.t.u-tokyo.ac.jp)

D. Yang, Department of Hydraulic Engineering, Tsinghua University, Beijing 100084, China.

K. Yang, Institute of Tibetan Plateau Research, Chinese Academy of Sciences, Beijing 100085, China.